



Article

Nanoporous Carbon Magnetic Hybrid Derived from Waterlock Polymers and Its Application for Hexavalent Chromium Removal from Aqueous Solution

Georgios Asimakopoulos ¹, Angeliki Karakassides ¹, Maria Baikousi ¹, Christina Gioti ¹,
Dimitrios Moschovas ¹, Apostolos Avgeropoulos ¹, Athanasios B. Bourlinos ², Alexios P. Douvalis ²,
Constantinos E. Salmas ¹ and Michael A. Karakassides ^{1,*}

¹ Department of Materials Science & Engineering, University of Ioannina, 45110 Ioannina, Greece; asimakopoulos.geo@gmail.com (G.A.); akarakasidou1@gmail.com (A.K.); mbaikou@uoi.gr (M.B.); christina.a.gioti@gmail.com (C.G.); dmoschov@uoi.gr (D.M.); aavger@uoi.gr (A.A.); ksalmas@uoi.gr (C.E.S.)
² Physics Department, University of Ioannina, 45110 Ioannina, Greece; bourlino@uoi.gr (A.B.B.); adouval@uoi.gr (A.P.D.)
* Correspondence: mkarakas@uoi.gr; Tel.: +30-26510-07276



Citation: Asimakopoulos, G.; Karakassides, A.; Baikousi, M.; Gioti, C.; Moschovas, D.; Avgeropoulos, A.; Bourlinos, A.B.; Douvalis, A.P.; Salmas, C.E.; Karakassides, M.A. Nanoporous Carbon Magnetic Hybrid Derived from Waterlock Polymers and Its Application for Hexavalent Chromium Removal from Aqueous Solution. *C* **2021**, *7*, 69. <https://doi.org/10.3390/c7040069>

Academic Editor: Gil Goncalves

Received: 31 August 2021

Accepted: 28 September 2021

Published: 30 September 2021

Publisher's Note: MDPI stays neutral with regard to jurisdictional claims in published maps and institutional affiliations.



Copyright: © 2021 by the authors. Licensee MDPI, Basel, Switzerland. This article is an open access article distributed under the terms and conditions of the Creative Commons Attribution (CC BY) license (<https://creativecommons.org/licenses/by/4.0/>).

Abstract: Sodium polyacrylate is the superabsorbent waterlock polymer used in disposable diapers, which are the third largest single consumer item in landfills. As diapers are difficult to recycle, their use produces an incredible amount of environmental waste. In the present article, we present a reliable and facile approach to transform sodium polyacrylate, the main constituent in the used diapers, in a carbon-based magnetic sorbent material, capable for use in environmental applications. A nanoporous carbon magnetic hybrid material was prepared by reacting NaPA with iron acetate species under chemical activation conditions. Analysis of the characterization results revealed, the creation of a nanoporous structure, with high specific surface area value ($S_{\text{BET}} = 611 \text{ m}^2/\text{g}$), along with the formation of nanosized zero valent iron nanoparticles and iron carbide (Fe_3C), inside the carbon pore system. ^{57}Fe Mössbauer spectroscopy verified also the existence of these two main iron-bearing phases, as well as additional minor magnetic phases, such as Fe_3O_4 and $\gamma\text{-Fe}_2\text{O}_3$. Vibrating sample magnetometry (VSM) measurements of the obtained hybrid confirmed its ferromagnetic/ferrimagnetic behavior. The hybrid material demonstrated a rapid sorption of Cr(VI) ions (adsorption capacity: 90 mg/g, 24 h, pH = 3). The results showed highly pH-dependent sorption efficiency of the hybrids, whereas a pseudo-second-order kinetic model described their kinetics.

Keywords: carbon; magnetic; nanoporous; superabsorbent polymers; hexavalent chromium; adsorption

1. Introduction

Superabsorbents (SAs) are defined as the materials which can absorb and hold large quantities of liquids, in comparison with their dry weight [1–3]. The most well-known material among them, is the sodium polyacrylate (NaPA), a super absorbent polymer (SAP), which structure is composed of very long carbon chains bonded with sodium atoms in repeating units, with the chemical formula of $-\text{CH}_2-\text{CH}(\text{COONa})$. When sodium polyacrylate is exposed to water, the higher concentration water molecules outside the polymer, attract the polar water molecules inside the polymer chains, via osmosis [4]. The NaPA swells and continues absorbing water until its concentration inside and outside the polymer coming to an equilibrium, while the initial material transforming into a hydrogel. Taking advantage of its ability to absorb as much as 400–800 times its mass in water, NaPA is used in many applications, such as: (i) absorbent for water and aqueous solutions in baby diapers, (ii) additive in surgical sponges, (iii) adult incontinence products and feminine hygiene products, (iv) thickening agent or sorbent infiltration units in industrial processes, and (v) water reservoir and soil amendment for agricultural uses [1,5–7].

On the other hand, the extensive use of NaPA especially in diapers, napkins, etc., as a superabsorbent component, has caused major environmental problems. These disposable products, form a sizeable portion of non-recyclable landfill waste, also contain many harmful chemicals that are subsequently scattered into the environment [8,9]. According to EPA (Environmental Protection Agency) the total number of produced disposable diapers per year in the USA were estimated about 27.5 billion, while the produced wastes that ended up in landfills were ~4.15 million tons (year 2017) [10]. Given this situation, large amounts of SAPs could be obtained from the castoff of above landfill wastes, which could be exploited as utility resources to prepare value-added products. Recently studies have shown that SAPs are very suitable precursors for the preparation of sponge-like activated carbons or porous carbon composites [11,12]. These SAPs contain, as well as carbon backbone chains and carboxylic groups, exchangeable metal ions, which serve as activating agents for a process that promotes stable carbon structures with an increased specific surface area and porosity. In addition, when the NaPA is placed in a solution containing other metal ions, i.e., Ca^{2+} , Ni^{2+} , Co^{2+} , Gr^{3+} , Fe^{3+} , etc., they preferentially bind to the anionic sites in the polymer, displacing the sodium ions and resulting in the formation of new hydrogels [13–16]. These types of hydrogels, which contain transition metal ions, seems to be suitable precursor for the fabrication of porous carbon structures decorated with oxides or metal nanoparticles.

Recently, there are many studies on the development of low-cost adsorbents based on carbon, namely by using waste materials for that purpose [17]. Activated carbon is the oldest and most widely used porous carbon material as adsorbent, used in a broad spectrum of applications, including water purification, remediation of polluted aquatic environments, gas storage, catalysis, medical and biomedical applications, etc. [18,19].

Furthermore, composite materials made by activated carbon or other type porous carbons and oxide/metal nanoparticles, have attracted a lot of interest for the remediation and treatment of water contaminated by heavy metal pollutants. The efficiency of these composites for environmental remediation is due to their higher reactivity and enhanced functionalities which are attributed to synergistic effects between matrix and nanoparticles. Among various types of nanoparticles that were investigated, magnetic iron and iron oxides have received considerable interest concerning the clean-up of environmental pollutants due to their small particle size, high surface area, catalytic activity, low cost, and simplicity of their production [20–23]. On the other hand, magnetic iron nanoparticles are sensitive in air oxidation and are easily formed in aggregations which decrease their effectiveness in environmental remediation. For these reasons, their stabilization into a host matrix is a big challenge for scientists because the nanoparticles could be protected and randomly dispersed without aggregations [24–27]. Moreover, the porous matrix should not only act as a supporting material, but also can also play an active role in the catalytic and sorption properties of the nanoparticle's system, especially when this particular combination of properties, could potentially generate novel hybrid materials, with better and/or new properties than the pristine materials.

Until now, there is a small number of studies regarding the development of carbon structures from carbonization of SAPs [11–13]. However, none of these studies utilized carbon/iron nanoparticle composites for environmental remediation processes. In the present work, we prepared a magnetic composite structure consisting of iron nanoparticles and porous carbon, using carbonization-chemical activation of iron polyacrylate, in conjunction with the ability of iron carboxylate compounds to transform upon pyrolysis into crystalline magnetic phases [28–30]. The structure of hybrid material was examined using X-ray diffraction (XRD), Fourier-transform (FT) Infrared thermal analysis methods, surface area measurements, and transmission electron microscopy (TEM). The nature of the nanoparticles and their magnetic behavior were examined employing Mössbauer spectroscopy, and magnetic measurements using vibrating sample magnetometer (VSM). Additionally, the hybrid was tested in comparison to pristine carbon for its ability to remove hexavalent chromium from aqueous solutions. This is the first time that such a hybrid material derived

from SAPs and consisting of magnetic nanoparticles, has been tested for environmental remediation and especially in hexavalent chromium removal. Chromium (Cr) is a widely used heavy metal in many engineering and chemical industries [31,32] but it is considered as a major pollutant on its oxidation state of Cr(VI). Cr(VI) is highly soluble and exerts toxic effects on humans and animals [33,34]. In the present study we present the ability of the new hybrid magnetic material in the Cr(VI) removal. Kinetic study was carried out using the pH and concentration of pollutants as parameters.

2. Materials and Methods

2.1. Reagents

All chemical reagents were used as purchased without further purification. Sodium polyacrylate, NaPA, cross-linked, iron(III) nitrate nonahydrate ($\text{Fe}(\text{NO}_3)_3 \cdot 9\text{H}_2\text{O}$), 1,5-diphenylcarbazide ($\text{C}_{13}\text{H}_{14}\text{N}_4\text{O}$, $\geq 97\%$), potassium dichromate ($\text{K}_2\text{Cr}_2\text{O}_7$, 99.98%), sodium hydroxide (NaOH, 97%) and phosphoric acid (H_3PO_4 , 85%) were purchased from Sigma-Aldrich. Potassium hydroxide (KOH, 85%) was purchased from Riedel-de Haen (Seelze, Germany) whereas hydrochloric acid (HCl, 37%), acetic acid (99.5%) and acetone (99.9%) from Merck. Finally, ethanol 99.5% (EtOH) and methanol 99.8% (MeOH) were supplied by Panreac (Barcelona, Spain).

2.2. Synthesis of Materials

3 g of NaPA was transferred in a 100 mL pyrex beaker, and then 80 mL solution of distilled water containing 3 g of $\text{Fe}(\text{NO}_3)_3 \cdot 9\text{H}_2\text{O}$, was added in the beaker at once. The NaPA immediately was transformed into a red-brown fluffy solid. The obtained solid, was dried for 1 h at 60 °C and then it was exposed to vapors of acetic acid at 80 °C for 1 h. The solid powder was dried again for 30 min at 80 °C to remove any physically absorbed acetic acid. Afterwards, the powder was mixed with the activating agent KOH (with weight ratio of 1:1) using an agate mortar for 5 min. Finally, the composite magnetic material was obtained after calcination for 30 min in Ar flowing atmosphere at 600 °C with 10 °C/min increment temperature rate (hereafter named NaPA@MAC). For comparison purposes, a sample of pure carbon was also prepared as a blank, using NaPA as the precursor and distilled water as swelling liquid. The final product (NaPA@C) was obtained under the same above carbonization conditions using KOH as activating agent (1:1).

2.3. Characterization of Materials

Infrared (FT-IR) spectra of samples in powder form, dispersed in KBr pellets, which were the average of 32 scans at 2 cm^{-1} resolution, were measured with a JASCO FT/IR-6000, Fourier transform spectrometer in the frequency range of 400–4000 cm^{-1} .

X-ray powder diffraction data were collected on a D8 Advance Bruker diffractometer using Cu K α (40 kV, 40 mA, $\lambda = 1.54178\text{ \AA}$) radiation and a secondary beam graphite monochromator. Diffraction patterns were collected in the 2θ range from 10 to 90 degrees, in steps of 0.02 degrees and 2 s counting time per step.

Thermogravimetric (TGA) and differential thermal analysis were performed using a Perkin Elmer Pyris Diamond TG/DTA. Samples of approximately 5 mg were heated in the air from 25 °C to 1000 °C, at a rate of 5 °C/min.

The ^{57}Fe Mössbauer spectrum of the NaPA@MAC was collected in transmission geometry at room temperature (300 K) using a constant-acceleration spectrometer, equipped with a $^{57}\text{Co}(\text{Rh})$ source kept at room temperature. Velocity calibration of the spectrometer was carried out using metallic $\alpha\text{-Fe}$ at 300 K and all isomer shift (IS) values are given relative to this standard. The experimentally recorded spectrum was fitted and analyzed using the IMSG code [35].

The magnetic properties of the NaPA@MAC were investigated by means of isothermal magnetization (M) versus (vs) applied magnetic field (H) measurements, which were conducted at room temperature using a vibrating sample magnetometer (VSM) (LakeShore 7300).

Transmission electron microscopy (TEM) observations were performed using the instrument JEM HR-2100, JEOL Ltd., Tokyo, Japan operated at 200 kV in bright-field mode. A drop of high-purity distilled water, containing the ultrasonically dispersed particles, was placed onto a holey carbon film supported by a copper-mesh TEM grid (CF300-CU-UL, carbon square mesh, CU, 300 mesh from Electron Microscopy Science, Hatfield, UK) and it was air-dried at room temperature.

Nitrogen porosimetry measurements were carried out at 77 K on a Quantachrome Autosorb iQ porosimeter using samples prior outgassed under vacuum (i.e., 10^{-6} mbar) at 120 °C for 10 h. The overall pore volume was calculated via the total adsorbed nitrogen amount at $P/P_0 = 0.998$ and the specific surface area was calculated using the BET, the Langmuir, and the CPSM model.

UV-Visible (UV-vis) spectra of solutions were measured in quartz cuvettes with a UV-2401(PC)-Shimadzu (Kyoto, Japan) two-beam spectrophotometer in the range 400–700 nm at a step of 0.5 nm using a halogen lamp.

2.4. Batch Experiments

The composite magnetic material NaPA@MAC has been used as adsorbent to remove Cr(VI) from aqueous solutions at temperature $T = 23$ °C. The effect to the adsorption, of pH value, initial Cr(VI) concentration and contact time were studied by different kinetic experiments. More specific, in order to study the effect of the pH to the adsorption capacity, 7.18 ppm Cr(VI) solutions with different pH value 1.5, 3.0, 4.5, 5.5, and 6.5 reacted with 180 mg/L NaPA@MAC for 24 h. The pH value was adjusted by adding 1 N HCl or NaOH whereas the Cr(VI) solutions were prepared by appropriate dilutions of a stock Cr(VI) solution (1 mg/mL). After 24 h, 3 mL of the suspensions were withdrawn, centrifuged and the Cr(VI) concentration was photometrically determined by applying the 1,5-diphenylcarbazide method [36]. The effect of the initial Cr(VI) concentration on the adsorption process was studied at pH 3 and different Cr(VI) solutions (0–300 mg Cr(VI)/gNaPA@MAC) while for the contact time effect, 7.18 ppm Cr(VI) solution at pH 3 was used. The Cr(VI) concentration of the solution was measured, at different time periods by following the method described above. A similar kinetic experiment also applied by using NaPA@C non-magnetic material as adsorbent, for comparison reasons.

3. Results and Discussion

3.1. Structural Characterization

Figure 1 displays the infrared spectrum of NaPA, NaPA@C, and the spectra of magnetic carbon derivative NaPA@MAC, before (a), and after treatment with the 48 ppm Cr(VI) solution for 24 h (b). All spectra show an intense and broad absorption band around 3420 cm^{-1} , corresponding to stretching vibrations of the free and intermolecular bonded hydroxyl groups. The OH-bending vibrations of the same groups appear at around 1630 cm^{-1} , overlapped with the vibrations' bands of carboxyl anions -COO^- ($\sim 1585\text{ cm}^{-1}$). The main features at high frequencies of the infrared spectrum of NaPA, consisting of three absorption bands at 2960, 2920, and 2850 cm^{-1} , which can be assigned [37,38] to the C–H asymmetric and symmetric stretching vibrations of the $(\text{-CH}_2\text{-})$ groups, of repeating polymeric unit. The same spectrum also exhibits two strong absorption maxima at around 1586 cm^{-1} and 1720 cm^{-1} . The first band could be assigned to the asymmetric stretching vibrations of -COO^- units, close to aromatic carbon rings, suggesting the presence of carboxylate groups, whereas the second band to the C=O stretching modes of protonated carboxylate groups which form cyclic dimers [39–43]. Furthermore, the band at 1450 cm^{-1} is attributed to symmetric stretching of -COO^- carbonyl, the band at 1165 cm^{-1} to C–O stretching vibrations, whereas the bands at 785 cm^{-1} and 855 cm^{-1} can be assigned to aromatic C–H out-of-plane bending vibrations [44–49].

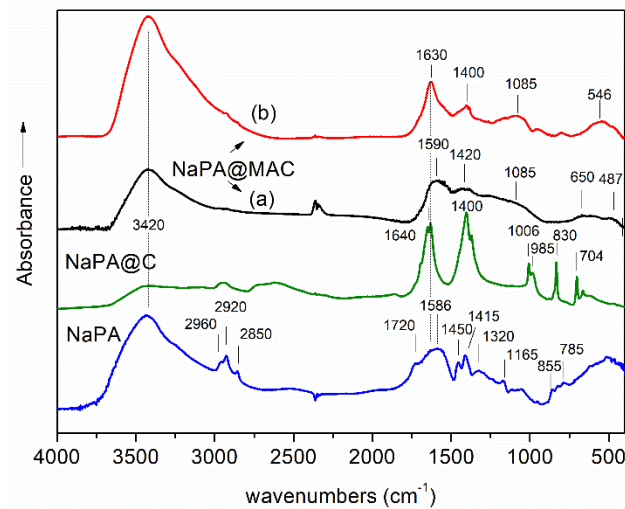


Figure 1. FT-Infrared spectra of samples: NaPA, NaPA@C, and NaPA@MAC before (a) and after treatment with the 48 ppm Cr(VI) solution for 24 h (b). Schemes follow the same formatting.

On the other hand, the infrared spectrum of sodium polyacrylate precursor after calcination (Figure 1 NaPA@C), exhibited two strong absorption bands at 1640 cm^{-1} and 1400 cm^{-1} and a significant number of weaker and sharper peaks at lower frequencies, i.e., 1006 cm^{-1} , 985 cm^{-1} , 830 cm^{-1} , and 704 cm^{-1} . All these bands could be attributed to KHCO_3 and K_2CO_3 , [50,51] which were formed during pyrolysis and decomposition of NaPA, in the presence of KOH activating agent. In fact, when KOH is used as chemical activator, several reactions may occur [52,53] such as:

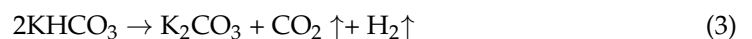


or



(carbonate or bicarbonate formation).

These compounds, are decomposed at higher temperatures according to reactions:



(carbonate or bicarbonate decomposition).

Furthermore, the spectrum (Figure 1 (a)) of untreated magnetic carbon derivative NaPA@MAC, is characteristic of carbon materials. In particular, the bands at 1590 cm^{-1} and 1165 cm^{-1} could be assigned to the stretching vibrations of $-\text{COO}^-$ units close to aromatic carbon rings and/or C–H bonds in aromatic carbon rings, respectively. The last one also was due to C–O single bonds, such as those in ethers, phenols, acids, and esters, while the broad band around 1085 cm^{-1} corresponds to the alcoholic C–O stretching vibration mode. The absorption at $\sim 1420\text{ cm}^{-1}$ corresponds to C–H bending and stretching vibration modes of $-\text{CH}_2$ groups. The formation of iron nanoparticles on carbon surfaces was also indicative from the spectrum of NaPA@MAC. For instance, at low frequency region ($745\text{--}500\text{ cm}^{-1}$), two broad bands observed at 650 cm^{-1} and 487 cm^{-1} , which were probably originated from Fe–O and Fe–C vibrations of the formed Fe_3C , oxidized iron and iron oxide nanoparticles. In fact, iron carbide (Fe_3C), oxide shell of zero valent iron (Fe^0), magnetite (Fe_3O_4) and maghemite ($\gamma\text{-Fe}_2\text{O}_3$), exhibit bands in the frequency range $650\text{--}450\text{ cm}^{-1}$, which could be assigned to the Fe–O and Fe–C stretching modes in their nanostructures [29,54,55]. Thus, the formation of such iron magnetic phases could be clearly suggested.

The spectrum of NaPA@MAC, after treatment with the 48 ppm Cr(VI) solution for 24 h is shown in Figure 1. The spectrum NaPA@MAC (b) exhibits strong absorption bands at

3420 cm^{-1} and 1630 cm^{-1} which were assigned to vibrations of adsorbed water molecules and two weak, in intensity, bands at 1410 cm^{-1} and 1085 cm^{-1} , due to C–O stretching and COO^- carbonyl stretching vibrations, respectively. According to literature [56], after Cr^{6+} was absorbed by porous carbons, the infrared absorbance was significantly decreased at around 1480 cm^{-1} . The proposed mechanism involves surface electron-donor groups of the adsorber such as carbonyls, hydroxyl, and aromatic π -conjugated systems to provide electrons to Cr^{6+} because of the strong affinities for Cr^{6+} under acidic conditions [57,58]. However, no significant differences in the frequency range 4000–1000 cm^{-1} could be observed between the spectra of NaPA@MAC carbon prior and after Cr^{6+} sorption, which suggested limited sorption of Cr^{6+} by the surface groups of magnetic carbon. In contrast, the spectrum of NaPA@MAC after Cr^{6+} sorption showed a significant increase in absorption at frequencies $< 700 \text{ cm}^{-1}$, indicative of the oxidation of zero-valent iron nanoparticles. Generally, the Cr^{6+} removal process by nZVI, involved initially the adsorption of hexavalent chromium anionic species on the active sites, and subsequently the stabilization and reduction, resulting in their precipitation on nZVI as Cr^{3+} -hydroxides and/or mixed $\text{Fe}^{3+}/\text{Cr}^{3+}$ -(oxy)hydroxides [59].

Figure 2 presents the powder XRD patterns within the 2θ range of 10–70°, of NaPA and NaPA@MAC samples. The X-ray diffraction pattern of NaPA carbon exhibited a very broad diffraction profile at low scattering angles ($2\theta < 30^\circ$), that along with the absence of sharp peaks in the whole pattern, revealed a predominantly amorphous structure of the sample.

On the other hand, the pattern of the NaPA@MAC exhibited several sharp and intense diffraction peaks, which suggested the formation of crystalline phases. Thus, the very intense well-defined peak at 44.8° and the weaker peak at 65.1° were assigned to reflections (110) and (200) of α -Fe crystalline phase, respectively (JCPD files no. 04-007-9753). From the full width at the half maximum (FWHM) of the more intense peak, at 44.8°, the average size of the zero-valent iron nanoparticles was estimated to be ~40 nm, using Scherrer's equation. In addition, on the same background there were also several weak peaks at 2θ , 37.8°, 39.9°, 40.8°, 43.0°, 43.8°, 45.9°, 48.7°, 49.3°, 52.0°, 57.0°, 58.1°, and 30.2°, 35.5°, 62.7°, probably corresponding to the crystalline phase of cementite (Fe_3C), (JCPD files no. 00-035-0772) and γ - Fe_2O_3 or Fe_3O_4 [JCPDS files no. 00-039-1346 and 01-086-1344], respectively, formed after pyrolysis in an inert atmosphere of ferric acetate-decorated NaPA sample [60]. The average size of Fe_3C nanoparticles was also estimated to be ~35 nm using Scherrer's equation.

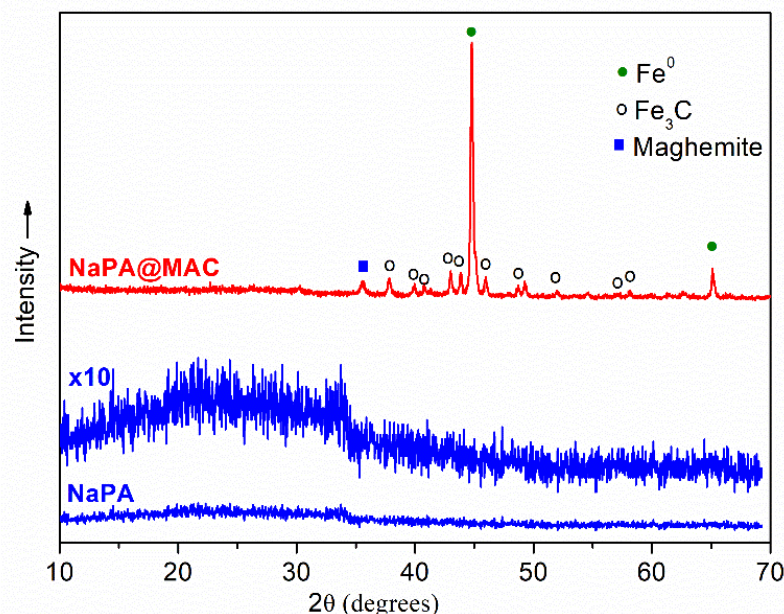


Figure 2. X-ray diffraction patterns of NaPA and NaPA@MAC samples.

Figure 3 shows the DTA/TG curves for the NaPA@C and NaPA@MAC samples. The DTA curves for both samples show several endothermic peaks at low temperatures (<200 °C), which could be attributed to the evaporation of adsorbed water and to the decomposition of potassium bicarbonate species formed during the pyrolysis of NaPA. Furthermore, the two curves also exhibited exothermic peaks between 370 and 420 °C, due to the partial combustion of the carbon matrix and endothermic peaks at ~750 °C, which could be assigned to K_2CO_3 decomposition.

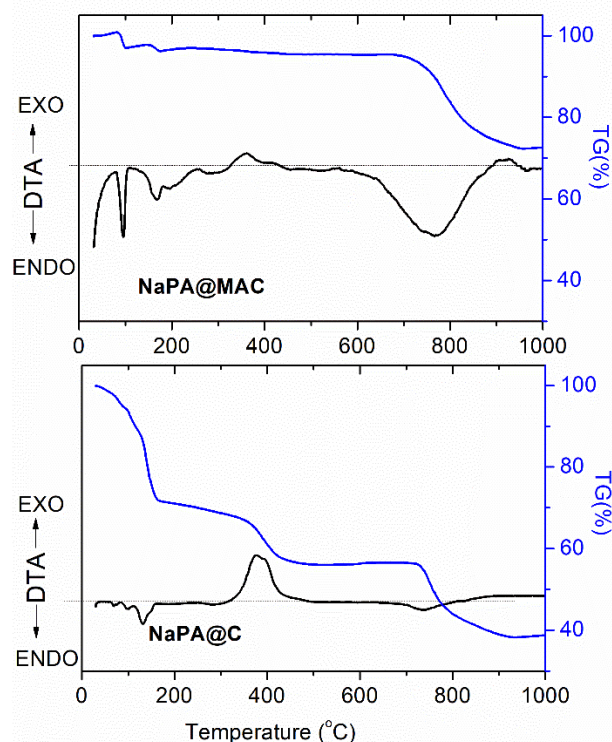


Figure 3. DTA and TGA curves of NaPA@C and NaPA@MAC samples.

The TGA curves for NaPA@C and NaPA@MAC samples are also shown in Figure 3, which illustrates the occurrence of three weight loss steps. These TG steps were correlated with the mass loss during heating of samples, and were attributed to processes such as dehydration, combustion, and decomposition. The NaPA@C sample showed a steep weight loss of nearly 62% between 25 °C and 900 °C due to the above-referred processes, whereas in the case of the NaPA@MAC, the TGA curve showed lower weight loss of about 28% for the same temperature range, that was attributed to the presence of thermal stable phase of Fe_3C , ZVI and magnetic iron oxides.

3.2. Textural, Surface, Morphological and Magnetic Properties

Figure 4 shows the transmission electron microscopy (TEM) bright field images of the NaPA@MAC hybrid in order to elucidate the morphology and arrangement of the nanophases. As shown in these images, nanoparticles (quasi-spherical in shape) with sizes between 3 and 8 nm, seems to be homogeneously dispersed on hybrid surfaces (Figure 4a,b). However, careful observation of the hybrid surfaces, revealed that some nanoparticles were accumulated in larger clusters ~40–50 nm in size (Figure 4c). It should be noted, that nanoparticles such as iron (Fe^0) and cementite (Fe_3C) due to their large energy densities, appeared with darker contrast in comparison to their adjacent phase of carbon or iron oxide nanoparticles [61–63]. Electron diffraction patterns of selected areas in the TEM images would have been a possibility to distinguish the three different forms of iron (zero valent iron, Fe_3C and iron oxide nanoparticles) but that has been exclusively studied and verified by XRD patterns and ^{57}Fe Mössbauer spectroscopy.

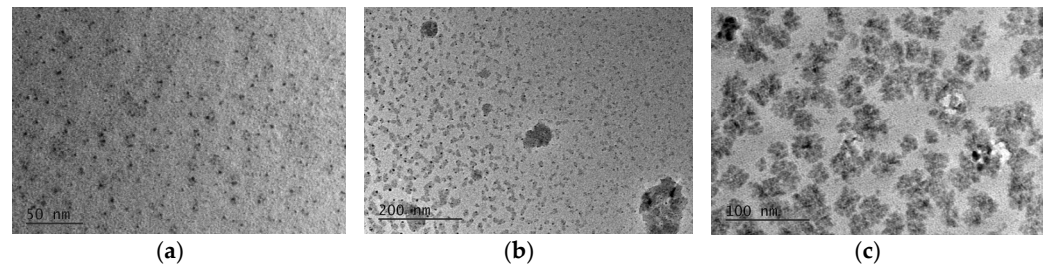


Figure 4. TEM images of NaPA@MAC hybrid with scale bar = 50 nm (a), 200 nm (b) and 100 nm (c).

According to the Figure 5a, it is obvious that the NaPA@MAC material exhibits a sharp knee in the low-pressure range (i.e., $P/P_0 < 0.01$) indicates the presence of microporosity ($D_{\text{micropore}} \leq 2$ nm). Moreover, it is obvious from the same figure that the NaPA@C prepared without iron magnetic particles exhibits a hysteresis loop with almost zero adsorbed nitrogen during nitrogen porosimetry measurements. This means practically zero pore specific surface area. In the first case, the knee is up to $110 \text{ cm}^3 \text{ STP/g}$ while the overall adsorbed volume is up to $440 \text{ cm}^3 \text{ STP/g}$ which corresponds to a percentage of 25%. Figure 5b illuminates the low relative pressure region (micropore region) for the case of magnetic material and presents the goodness of fitting of the experimental data by the CPSM model [64,65]. The micropore volume fraction predicted by the CPSM model fitting on the overall hysteresis loop is 21.4% while the Dubinin–Raduskevitch (D–R) method [66] predicts a micropore volume fraction of 32.2%. More specifically, as it is reported in Table 1, according to the CPSM model [64,65] the micropore volume is $0.146 \text{ cm}^3/\text{g}$ and according to the Dubinin–Raduskevitch (D–R) method [66] the micropore volume is $0.220 \text{ cm}^3/\text{g}$. The pore volume distribution (Figure 5c), provided by the application of the CPSM and the DFT model [67] on the magnetic material experimental data, indicates the presence of two separated groups of pores, one with mean pore diameter around $D = 1.70$ nm and $D = 1.67$ nm, and one with mean pore diameter around $D = 2.90$ nm and $D = 2.52$ nm for the CPSM and the DFT model, respectively. Furthermore, it is obvious from the same figure that pore diameters are extended beyond the size of 5 nm and this observation is supported by both the CPSM and the DFT model. On the other hand, the pore number distribution (pore population distribution) (Figure 5d) provided by the CPSM model indicates that 63% of pores are in the micropore region ($D \leq 2.0$ nm). The perfect simulation of the nitrogen porosimetry process by the CPSM model also provides results for specific surface area values as follows, $S_{\text{BET}} = 611 \text{ m}^2/\text{g}$, $S_{\text{Langmuir}} = 796 \text{ m}^2/\text{g}$, and $S_{\text{CPSM}} = 729 \text{ m}^2/\text{g}$ (Table 2). The presence of microporosity introduces the pore curvature effect on specific surface area calculations [68] which means that the CPSM model predictions, which are between the BET and Langmuir predictions, are more realistic.

Table 1. Pore structure characterization results derived from Dubinin–Raduskevitch (D–R) method, DFT model, and the simulation of the overall N_2 adsorption–desorption hysteresis loop by CPSM model.

Sample Code	V_{pore} (cm^3/g)	$V_{\text{micro}}^{\text{D-R}}$ (cm^3/g)	$V_{\text{micro}}^{\text{CPSM}}$ (% cm^3/g)	$D_{\text{Nmean}}^{\text{CPSM}}$ (nm)	$D_{\text{Vmean}}^{\text{CPSM}}$ (nm)	$D_{\text{Vmean}}^{\text{DFT}}$ (nm)
NaPA@MAC	0.682	0.220	0.146	1.69	1.70, 2.90	1.67, 2.52, 5.01

Table 2. Specific Surface Area (SSA) estimation derived from the classic models BET and Langmuir as well as from the CPSM model.

Sample Code	S_{gBET} (m^2/g)	C_{BET}	$S_{\text{gLang.}}$ (m^2/g)	$C_{\text{Lang.}}$	S_{CPSM} (m^2/g)
NaPA@MAC	611	372	796	55	729

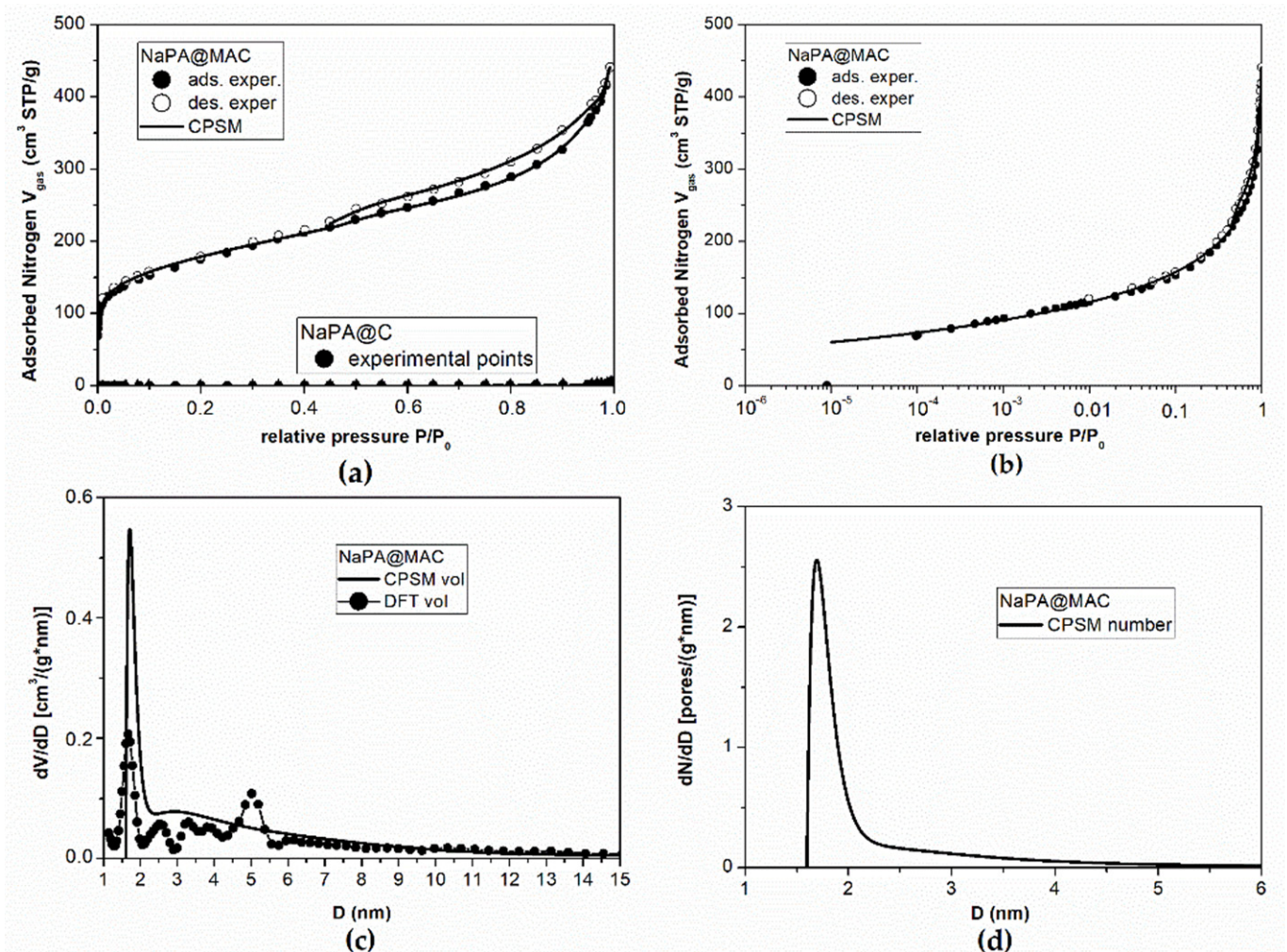


Figure 5. Simulation and results of nitrogen porosimetry experimental data for NaPA@MAC and NaPA@C materials. CPSM model fitting (continuous line) over all the experimental adsorption (black points) and desorption (white points) data (a) higher relative pressure hysteresis loop for the material prepared with NaPA@MAC and without magnetic iron particles NaPA@C (b) lower relative pressure hysteresis loop for NaPA@MAC. (c) Pore volume distribution according to the DFT (black points) and to the CPSM (black line) for NaPA@MAC. (d) Pore number (population) distribution according to the CPSM model for NaPA@MAC.

The room temperature ^{57}Fe Mössbauer spectrum of NaPA@MAC is presented in Figure 6 and shows a combination of several magnetically split components (sextets). In particular, a set of four clearly magnetically resolved sextets and a broad magnetically split contribution were used to fit this spectrum adequately. The resulting Mössbauer parameters values for these components are listed in Table 3. From these values it is clear that the two major contributions (regarding their absorption areas) correspond to a metallic $\alpha\text{-Fe}$ and a carbide Fe_3C phase and the two minor clearly resolved sextets with large hyperfine magnetic field (B_{hf}) values to the mixed valence iron spinel oxide magnetite (Fe_3O_4) phase [69]. The fifth broad component presents Mössbauer parameters values that are characteristic of an assembly of superparamagnetic (SPM) magnetite or oxidized magnetite ($\text{Fe}_{3-x}\text{O}_4$) nanoparticles phase.

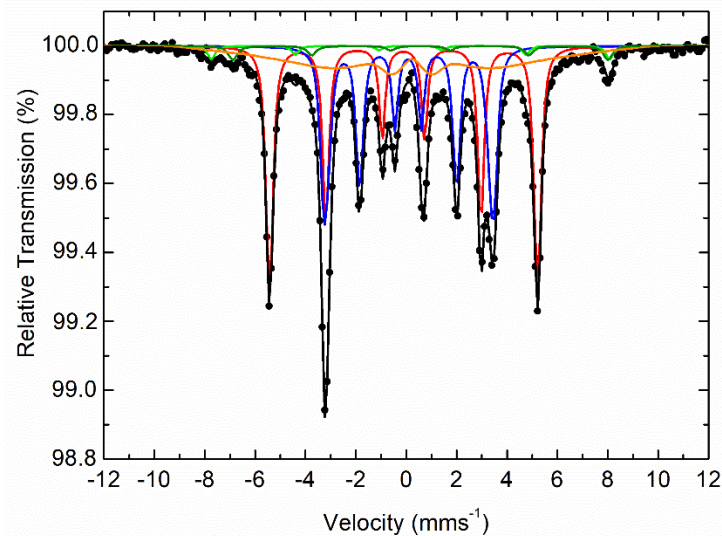


Figure 6. Room temperature ^{57}Fe Mössbauer spectrum of NaPA@MAC hybrid. Color curves are defined in Table 3.

Table 3. ^{57}Fe Mössbauer hyperfine parameters resulting from the best fits of the corresponding spectrum of NaPA@MAC sample recorded at 300 K. IS is the isomer shift (given relative to $\alpha\text{-Fe}$ at 300 K), $\Gamma/2$ is the half line-width, 2ϵ is the quadrupole shift, B_{hf} is the central value of the hyperfine magnetic field, ΔB_{hf} is the spreading of B_{hf} , and Area is the relative spectral absorption area of each component used to fit the spectrum. Typical errors are ± 0.02 mm/s for IS, $\Gamma/2$, and 2ϵ , ± 3 kOe for B_{hf} and $\pm 5\%$ for Area.

Component (Color)	IS (mm/s)	$\Gamma/2$ (mm/s)	2ϵ (mm/s)	B_{hf} (kOe)	ΔB_{hf} (kOe)	Area (%)
$\alpha\text{-Fe}$ (red)	0.00	0.14	0.01	331	4	39
Fe_3C (blue)	0.20	0.14	0.03	211	7	34
Fe^{3+} (Fe_3O_4) (green)	0.28	0.17	0.00	491	0	2
$\text{Fe}^{2.5+}$ (Fe_3O_4) (olive)	0.67	0.21	0.00	462	0	3
SPM $\text{Fe}_3\text{O}_4/\text{Fe}_{3-x}\text{O}_4$ (orange)	0.34	0.14	0.01	290	72	22

Figure 7 presents the M vs H loop measurements of the NaPA@MAC sample collected at room temperature. The clear ferromagnetic characteristics of this loop reflect the contributions from the ferromagnetic ($\alpha\text{-Fe}$, Fe_3C) and ferrimagnetic (Fe_3O_4) phases present in the sample [70,71]. In particular, the saturation magnetization of ~ 47 Am^2/kg reflects the hybrid nature of the sample, while the coercivity of ~ 14 mT the contribution of the nanostructured nature of the magnetic phases in the sample.

3.3. Sorption Kinetic Study for Cr^{6+} Removal from Aqueous Solution

Figure 8a shows that for pH values in the range 1–3 (acidic environment), 100% of the Cr(VI) amount in a 7.18 ppm solution was adsorbed by the NaPA@MAC material after 24 h and for temperature $T = 23$ °C. Furthermore, for pH values in the range of 4.5–6.5, the % Cr(VI) adsorbed amount almost reaches the value of 0%. For this reason, experiments for the estimation of maximum adsorption capacity, and for the effect of the initial Cr(VI) concentration on this capacity, were carried out at pH = 3 and $T = 23$ °C for 24 h with different initial Cr(VI) concentrations. It is obvious from Figure 8b that for $C_{\text{init}} = 143$ $\text{mg}_{\text{Cr(VI)}}/\text{g}_{\text{AC}}$ (i.e., 25.72 ppm) the experimental maximum adsorbed amount after 24 h of the adsorption process is $q_{\text{max}}(24 \text{ h}) = 55.3$ $\text{mg}_{\text{Cr(VI)}}/\text{g}_{\text{AC}}$ while for $C_{\text{init}} = 298$ $\text{mg}_{\text{Cr(VI)}}/\text{g}_{\text{AC}}$ (i.e., 53.67 ppm) the experimental maximum adsorbed amount after 24 h of the adsorption process is $q_{\text{max}}(24 \text{ h}) = 92$ $\text{mg}_{\text{Cr(VI)}}/\text{g}_{\text{AC}}$. This means that the maximum adsorption capacity is strongly ruled by the initial Cr(VI) concentration at least

for a value of $C_{\text{init}} \leq 53$ ppm. The trend of this graph (i.e. Figure 8b) shows that for higher Cr(VI) initial concentration a higher maximum adsorption capacity will be achieved.

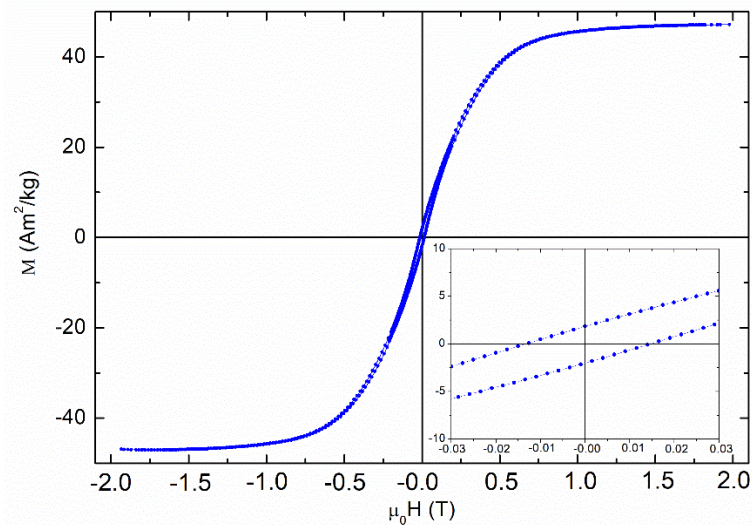


Figure 7. M vs H loop of NaPA@MAC sample recorded at room temperature. The inset presents a magnification focused on the loop's center to reveal the coercive characteristics.

A kinetic experiment with initial Cr(VI) concentration of 7.18 ppm, was carried out at pH = 3 and T = 23 °C for 24 h. Measurements were carried out for both material prepared with and without magnetic iron particles. In the case that magnetic iron particles weren't used, Figure 9b, the total adsorbed Cr(VI) amount is zero. This is expected according to Figure 5a because of the zero-pore specific surface area. Pseudo First Order kinetic model (PFO), Pseudo Second Order kinetic model (PSO), and Diffusion–Chemisorption kinetic model (DC) were tested on material prepared using magnetic iron particles, to resort to the most suitable mechanism of adsorption [72]. Results are reported in Table 4.

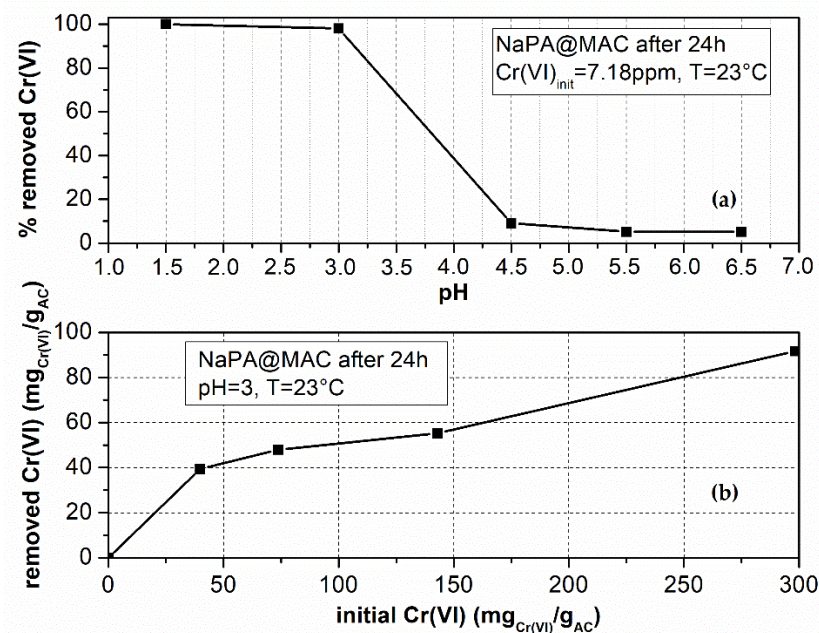


Figure 8. (a) Effect of pH on maximum removed Cr(VI) for the NaPA@MAC material. (b) Effect of initial Cr(VI) concentration on maximum removed Cr(VI) amount after 24 h for pH = 3 and T = 23 °C.

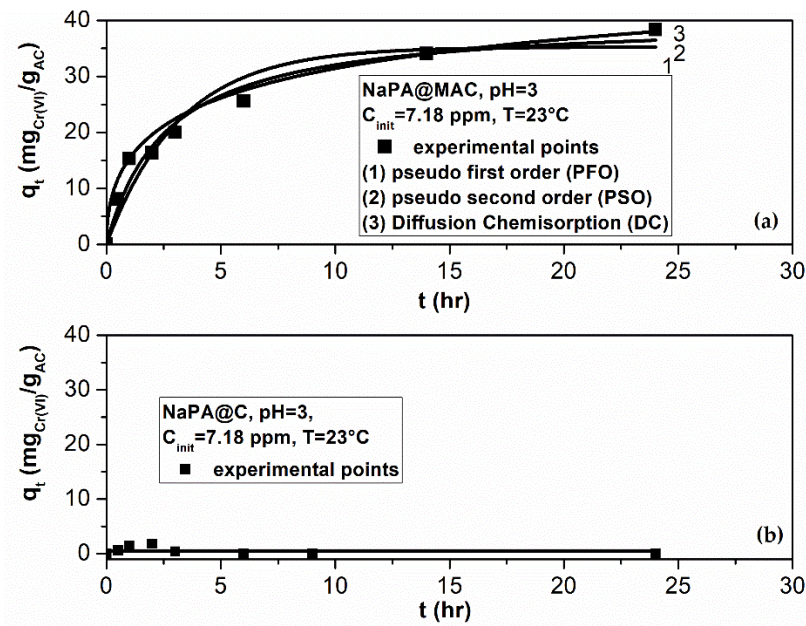


Figure 9. A 24h experiment for the kinetic behavior of Cr(VI) removal via adsorption on (a) NaPA@MAC and (b) NaPA@C, at pH = 3, T = 23 °C and for $C_{init} = 7.18$ ppm Cr(VI). Best fit of three kinetic models on adsorption process experimental data for the case (a).

Table 4. R^2 correlation coefficient values, k specific reaction rate values, and q_e adsorbed amount at the equilibrium stage, which are provided by Levenberg–Marquardt Least-Square fitting algorithm upon the NaPA@MAC kinetic experimental dataset.

NaPA@MAC (7.18 ppm)	PFO	PSO	DC
R^2	0.9249	0.9657	0.9136
k	0.3119	0.0095	20.41
q_e	35.25	40.43	61.27

It is obvious from Figure 9, that after 24 h, the NaPA@MAC material tend to vanish the Cr(VI) at this initial concentration (i.e. $39.9 \text{ mg}_{\text{Cr(VI)}}/\text{g}_{\text{AC}}$). Furthermore, as it is shown in Table 4 the Cr(VI) adsorbed amount at the equilibrium stage (i.e. after infinite time, when the solid material will be saturated), is estimated to be over $61 \text{ mg}_{\text{Cr(VI)}}/\text{g}_{\text{AC}}$ according to the Diffusion–Chemisorption (DC) model and over $40 \text{ mg}_{\text{Cr(VI)}}/\text{g}_{\text{AC}}$ according to the pseudo second order (PSO) model. The R^2 parameter of the Levenberg–Marquardt Least-Square fitting algorithm which are also presented in Table 4 was the tool for the evaluation of such models in our case. The R^2 of the Pseudo First Order (PFO) model and of the Diffusion–Chemisorption (DC) model falls off. This means that for $C_{init} = 7.18$ ppm (a low initial concentration), the occupation by Cr(VI) or other elements of the unoccupied sites in the pores is not the controlling stage (PFO mechanism [72]). Before the Cr(VI) consumed totally, saturation or transient phenomenon starts. A high percentage of the active sites of the pore surface were occupied quickly during initial time moments, but when this initial time pass, phenomena such as transient adsorption, chemisorption, Van der Waals bonding, ion exchange, reaction, etc., start to exist in pores. One of the basic principles of the PSO model is that chemisorption phenomena are the controlling mechanism [72]. To check out if the PSO is the only biosorption active rate limiting mechanism we fitted the experimental data using the Diffusion–Chemisorption (DC) model [72]. According to the R^2 values which are presented in Table 4 this model exhibits a not so good fitting capability compared to this of the PSO model.

According to all of the above-mentioned points, neither the collision of the adsorbed molecules with the unoccupied pore surface sites nor the diffusion through pores are

the only controlling mechanism [73]. For this reason, the Pseudo Second Order (PSO) model seems to be the most appropriate for the kinetic study of this work. This model indicates a more complex mechanism involving both the above-mentioned controlling stages plus a surface bonding process which occurs on the pore surface sites and may be a reaction on the surface of pores. Furthermore, according to this model, the state of the adsorbate, i.e., liquid or gas, and the pore size distribution of the activated carbon are strongly interactive [74]. In the case of liquid media as an adsorbate (our case), the existence of micropores in combination with the existence of meso and macro pores is more effective for such adsorption processes [73]. In our case, according to the CPSM model [64,65], and according to the results presented in Figure 5d, the NaPA@MAC exhibits a population of approximately 37% macro-meso pores which contributes to the relatively quick intraparticle diffusion and a population of approximately 63% micropores which contributes to the relatively slow diffusion and transient adsorption, the surface bonding, the chemisorption, and the surface reactions [73].

Finally, Table 5 presents a comparison between the adsorption capacities of various adsorbents reported in the literature for the removal of Cr(VI). It is observed that NaPA@MAC has higher or comparable adsorption efficiency than other activated carbons, magnetic activated carbon hybrids or bare iron-based nanoparticles.

Table 5. Adsorption capacities (q_m) of Cr(VI) on NaPA@MAC and other adsorbents reported in the literature.

	pH	q_m (mg/g)	Ref.
AC_fiber/nZVI	3	91.5	[75]
AC(Filtrisorb-400)/nZVI	4	25	[76]
AC/nZVI	5	24	[77]
AC-tires	2	58.5	[78]
nZVI-MAC	4	66	[79]
AC-tires waste/magnetic iron oxides	2	49.3	[80]
Corn cob-derived magnetic AC	2	57	[81]
PAC-Fe ⁰ /Ag	3	100	[82]
nZVI-Fe ₃ O ₄ nanocomposites	3	100	[83]
Maghemite nanoparticles	2.5	19.4	[84]
δ -FeOOH-coated γ -Fe ₂ O ₃	2.5	25.8	[84]
Powdered AC	4	46.9	[85]
AC <i>Hevea brasiliensis</i> (rubberwood) sawdust	2	44.05	[86]
AC coconut tree sawdust	3	3.46	[87]
AC longan seed	3	35.02	[88]
AC Casuarina equisetifolia leaves	3	17.2	[89]
AC-Poseidonia Oceanica	3	120	[90]
AC-spent coffee	3	109	[91]
Fe/Fe ₃ C nanoparticles	3	100	[92]
AC/Fe-Fe ₃ O ₄	2–6	165–73	[93]
NaPA@MAC	3	90	This work

4. Conclusions

A porous carbon magnetic hybrid (NaPA@MAC) comprised of magnetic iron species such as Fe⁰, Fe₃C, magnetite and/or maghemite nanoparticles immobilized onto a porous carbon has been prepared, characterized, and tested for Cr(VI) treatment. The porous carbon phase was derived from the pyrolysis of sodium polyacrylate, a superabsorbent polymer used in disposable diapers. The development of nanoparticles was based on the affinity of acetic acid vapors to react with the dispersed iron cations in the supporting phase to first form iron acetate precursor species which further produce the magnetic nanoparticles upon pyrolysis. FT-IR, XRD, and TEM measurements revealed the formation of dispersed magnetic iron and iron-bearing nanoparticles on porous carbon surfaces, which exhibit typical surface chemistry of activated carbon materials. The major part of Fe⁰ and Fe₃C nanoparticles were homogeneously dispersed on the hybrid surfaces (with mean particle size ~6 nm) or they were accumulated in larger clusters of ~40–50 nm in size. Magnetization (*M*) vs magnetizing field (*H*) loop measurements showed a clear ferromagnetic behavior of the hybrid with a saturation magnetization of ~47 Am²/kg, originated from the contributions from the ferromagnetic (Fe⁰, Fe₃C) and ferrimagnetic (Fe₃O₄) phases present in the sample. Using various models and methods the surface area of magnetic hybrid was calculated to be between 611 and 796 m²/g, the total pore volume ~0.68 cm³/g, whereas the micropore volume was calculated at about ~0.220 cm³/g. Pore size distribution analysis of the hybrid, indicated the presence of two separated groups of pores, one with a mean diameter around 1.70 nm, and one with a diameter ~2.90 nm, respectively. The adsorption kinetics data were fitted with the pseudo second-order model which seems to be the most appropriate for the kinetic study of this work. Due to the specific surface properties of NaPA@MAC and synergic effects of both counterparts, the material exhibits extremely high efficiency for Cr(VI) removal which at pH equals 3 and after 24 h of the adsorption process was ~92 mg/g whereas the 100% of Cr(VI) amount was adsorbed by the hybrid when the chromium initial concentration was 7.18 ppm.

Author Contributions: Conceptualization, M.A.K. and A.B.B.; Methodology, M.A.K., A.B.B. and A.K.; Formal Analysis, M.A.K., C.E.S. and A.P.D.; Investigation, G.A., A.K., M.B., C.G., D.M. and A.A.; Resources, M.A.K.; Writing—Original Draft Preparation, M.A.K., C.E.S. and A.P.D.; Writing—Review and Editing, M.A.K., A.B.B., C.E.S. and M.B.; Visualization, M.A.K., C.E.S. and A.P.D.; Supervision, M.A.K. and A.B.B.; Project Administration, M.A.K.; Funding Acquisition, M.A.K. All authors have read and agreed to the published version of the manuscript.

Funding: This study was funded by the project “National Infrastructure in Nanotechnology, Advanced Materials and Micro-/Nanoelectronics” (MIS-5002772) which was implemented under the action “Reinforcement of the Research and Innovation Infrastructure”, funded by the Operational Programme “Competitiveness, Entrepreneurship and Innovation” (NSRF 2014–2020), and co-financed by Greece and the European Union (European Regional Development Fund).

Data Availability Statement: The data presented in this study are available on request from the corresponding author.

Acknowledgments: The authors greatly acknowledge Ch. Papachristodoulou for the XRD measurements and the use of the XRD and VSM Laboratory Network Units of the University of Ioannina.

Conflicts of Interest: The authors declare no conflict of interest.

References

1. Mignon, A.; De Belie, N.; Dubruel, P.; Van Vlierberghe, S. Superabsorbent polymers: A review on the characteristics and applications of synthetic, polysaccharide-based, semi-synthetic and ‘smart’ derivatives. *Eur. Polym. J.* **2019**, *117*, 165–178. [[CrossRef](#)]
2. Mudiyansele, T.K.; Neckers, D.C. Highly Absorbing Superabsorbent Polymer. *J. Polym. Sci. A Polym. Chem.* **2008**, *46*, 1357–1364. [[CrossRef](#)]
3. Ma, X.; Wen, G. Development history and synthesis of super-absorbent polymers: A review. *J. Polym. Res.* **2020**, *27*, 136. [[CrossRef](#)]
4. Mahon, R.; Balogun, Y.; Oluyemi, G.; Njuguna, J. Swelling performance of sodium polyacrylate and poly(acrylamide-co-acrylic acid) potassium salt. *SN Appl. Sci.* **2020**, *2*, 117. [[CrossRef](#)]

5. Behera, S.; Mahanwar, P.A. Superabsorbent polymers in agriculture and other applications: A review. *Polym.-Plast. Technol. Mater.* **2020**, *59*, 341–356. [[CrossRef](#)]
6. Hüttermann, A.; Orikiriza, L.J.B.; Agaba, H. Application of Superabsorbent Polymers for Improving the Ecological Chemistry of Degraded or Polluted Lands. *Clean* **2009**, *37*, 517–526. [[CrossRef](#)]
7. Wyrzykowski, M.; Lura, P. Controlling the coefficient of thermal expansion of cementitious materials—A new application for superabsorbent polymers. *Cem. Concr. Compos.* **2013**, *35*, 49–58. [[CrossRef](#)]
8. Umachitra, G.; Bhaarathidurai. Disposable baby diaper—A threat to the health and environment. *J. Environ. Sci. Eng.* **2012**, *54*, 447–452.
9. Wong, D.L.; Brantly, D.; Clutter, L.B.; De Simone, D.; Lammert, D.; Nix, K.; Perry, K.A.; Smith, D.P.; White, K.H. Diapering choices: A critical review of the issues. *Pediatr. Nurs.* **1992**, *18*, 41–54.
10. EPA, United States Environmental Protection Agency. Nondurable Goods: Product-Specific Data. Available online: <https://www.epa.gov/facts-and-figures-about-materials-waste-and-recycling/nondurable-goods-product-specific-data#DisposableDiapers> (accessed on 31 August 2021).
11. Wu, J.; Tao, K.; Kang, L.; Jiang, H.; Zhang, D.; Xu, S.; Wang, B. Preparation of sponge-like activated carbon via carbonization of super absorbent polymer (SAP) as electrode materials for supercapacitors. *Fuller. Nanotub. Carbon NanoStruct.* **2016**, *24*, 635–640. [[CrossRef](#)]
12. Meng, F.; Fan, X.; Xing, A.; Liu, H.; Lin, C.; Wang, Z.; Xu, L.; Zheng, L.; Liu, J. Sodium polyacrylate-derived porous carbon nanosheets for high performance lithium-sulfur batteries. *Sustain. Energy Fuels* **2019**, *3*, 942–947. [[CrossRef](#)]
13. Lu, B.-Q.; Zhu, Y.-J.; Zhao, X.-Y.; Cheng, G.-F.; Ruan, Y.-J. Sodium polyacrylate modified Fe₃O₄ magnetic microspheres formed by self-assembly of nanocrystals and their applications. *Mater. Res. Bull.* **2013**, *48*, 895–900. [[CrossRef](#)]
14. Horkay, F.; Bassar, P.J.; Hecht, A.-M.; Geissler, E. Effect of calcium/sodium ion exchange on the osmotic properties and structure of polyelectrolyte gels. *Proc. Inst. Mech. Eng. Part H J. Eng. Med.* **2015**, *229*, 895–904. [[CrossRef](#)] [[PubMed](#)]
15. Ouass, A.; Kadiri, L.; Essaadaoui, Y.; Belakhmima, R.A.; Cherkaoui, M.; Lebkiri, A.; Rifi, E.H. Removal of trivalent chromium ions from aqueous solutions by Sodium polyacrylate beads. *Mediterr. J. Chem.* **2018**, *7*, 125–134. [[CrossRef](#)]
16. Huang, Y.; Liu, J.; Wang, J.; Hu, M.; Mo, F.; Liang, G.; Zhi, C. An Intrinsically Self-Healing NiCo | Zn Rechargeable Battery with a Self-Healable Ferric-Ion-Crosslinking Sodium Polyacrylate Hydrogel Electrolyte. *Angew. Chem.* **2018**, *57*, 9810–9813. [[CrossRef](#)] [[PubMed](#)]
17. Dias, J.M.; Alvim-Ferraz, M.C.M.; Almeida, M.F.; Rivera-Utrilla, J.; Sanchez-Polo, M. Waste materials for activated carbon preparation and its use in aqueous-phase treatment: A review. *J. Environ. Manag.* **2007**, *85*, 833–846. [[CrossRef](#)] [[PubMed](#)]
18. Marsh, H.; Rodríguez-Reinoso, F. *Activated Carbon*; Elsevier Science Ltd.: Oxford, UK, 2006; ISBN 9780080455969.
19. Danish, M.; Ahmad, T. A review on utilization of wood biomass as a sustainable precursor for activated carbon production and application. *Renew. Sustain. Energy Rev.* **2018**, *87*, 1–21. [[CrossRef](#)]
20. Laurent, S.; Forge, D.; Port, M.; Roch, A.; Robic, C.; Vander Elst, L.; Muller, R.N. Magnetic Iron Oxide Nanoparticles: Synthesis, Stabilization, Vectorization, Physicochemical Characterizations, and Biological Applications. *Chem. Rev.* **2008**, *108*, 2064–2110. [[CrossRef](#)]
21. Kudr, J.; Haddad, Y.; Richtera, L.; Heger, Z.; Cernak, M.; Adam, V.; Zitka, O. Magnetic Nanoparticles: From Design and Synthesis to Real World Applications. *Nanomaterials* **2017**, *7*, 243. [[CrossRef](#)]
22. Ali, A.; Zafar, H.; Zia, M.; Haq, I.; Phull, A.R.; Ali, J.S.; Hussain, A. Synthesis, characterization, applications, and challenges of iron oxide nanoparticles. *Nanotechnol. Sci. Appl.* **2016**, *9*, 49–67. [[CrossRef](#)]
23. Bae, S.; Collins, R.N.; Waite, T.D.; Hanna, K. Advances in Surface Passivation of Nanoscale Zerovalent Iron: A Critical Review. *Environ. Sci. Technol.* **2018**, *52*, 12010–12025. [[CrossRef](#)]
24. Pan, B.; Chen, D.; Zhang, H.; Wu, J.; He, F.; Wang, J.; Chen, J. Stability of hydrous ferric oxide nanoparticles encapsulated inside porous matrices: Effect of solution and matrix phase. *Chem. Eng. J.* **2018**, *347*, 870–876. [[CrossRef](#)]
25. Shi, J.; Wang, J.; Wang, W.; Teng, W.; Zhang, W.-X. Stabilization of nanoscale zero-valent iron in water with mesoporous carbon (nZVI@MC). *J. Environ. Sci.* **2019**, *81*, 28–33. [[CrossRef](#)] [[PubMed](#)]
26. Shiva, K.; Jayaramulu, K.; Hb, R.; Maji, T.; Bhattacharyya, A. In-situ Stabilization of Tin Nanoparticles in Porous Carbon Matrix derived from Metal Organic Framework: High Capacity and High Rate Capability Anodes for Lithium-ion Batteries. *Z. Anorg. Allg. Chem.* **2014**, *640*, 1115–1118. [[CrossRef](#)]
27. Zhang, D.; Wei, S.; Kaila, C.; Su, X.; Wu, J.; Karki, A.B.; Young, D.P.; Guo, Z. Carbon-stabilized iron nanoparticles for environmental remediation. *Nanoscale* **2010**, *2*, 917–919. [[CrossRef](#)] [[PubMed](#)]
28. Jewur, S.S.; Kuriacose, J.C. Studies on thermal decomposition of ferric acetate. *Thermochim. Acta* **1977**, *19*, 195–200. [[CrossRef](#)]
29. Baikousi, M.; Bourlinos, A.B.; Douvalis, A.; Bakas, T.; Anagnostopoulos, D.F.; Tucček, J.; Sáfářová, K.; Zbořil, R.; Karakassides, M.A. Synthesis and Characterization of γ -Fe₂O₃/Carbon Hybrids and Their Application in Removal of Hexavalent Chromium Ions from Aqueous Solutions. *Langmuir* **2012**, *28*, 3918–3930. [[CrossRef](#)] [[PubMed](#)]
30. Karakassides, M.A.; Gournis, D.; Bourlinos, A.B.; Trikalitis, P.N.; Bakas, T. Magnetic Fe₂O₃-Al₂O₃ composites prepared by a modified wet impregnation method. *J. Mater. Chem.* **2003**, *13*, 871–876. [[CrossRef](#)]
31. Pariser, H.H.; Backeberg, N.R.; Masson, O.C.M.; Bedder, J.C.M. Changing nickel and chromium stainless steel markets—A review. *J. S. Afr. Inst. Min. Metall.* **2018**, *118*, 563–568. [[CrossRef](#)]

32. Dakiky, M.; Khamis, M.; Manassra, A.; Mer'eb, M. Selective adsorption of chromium (VI) in industrial wastewater using low-cost abundantly available adsorbents. *Adv. Environ. Res.* **2002**, *6*, 533–540. [[CrossRef](#)]
33. Sun, H.; Brocato, J.; Costa, M. Oral Chromium Exposure and Toxicity. *Curr. Environ. Health Rep.* **2015**, *2*, 295–303. [[CrossRef](#)]
34. Barceloux, D.G. Chromium. *J. Toxicol. Clin. Toxicol.* **1999**, *37*, 173–194. [[CrossRef](#)] [[PubMed](#)]
35. Douvalis, A.; Polymeros, A.; Bakas, T. IMMSG09: A $^{57}\text{Fe}/^{119}\text{Sn}$ Mössbauer spectra computer fitting program with novel interactive user interface. *J. Phys. Conf. Ser.* **2010**, *217*, 012014. [[CrossRef](#)]
36. Clesceri, L.S.; Greenberg, A.E.; Eaton, A.D. *Standard Methods for the Examination of Water and Wastewater*, 20th ed.; American Public Health Association: Washington, DC, USA, 1998; pp. 3–71.
37. Fearheller, W.R.; Katon, J.E. The vibrational spectra of acrylic acid and sodium acrylate. *Spectrochim. Acta A Mol. Biomol. Spectrosc.* **1967**, *23*, 2225–2232. [[CrossRef](#)]
38. Grabowska, B.; Holtzer, M. Structural examination of the cross-linking reaction mechanism of polyacrylate binding agents. *Arch. Metall. Mater.* **2009**, *54*, 427–437.
39. Dandekar, A.; Baker, R.T.K.; Vannice, M.A. Characterization of activated carbon, graphitized carbon fibers and synthetic diamond powder using TPD and DRIFTS. *Carbon* **1998**, *36*, 1821–1831. [[CrossRef](#)]
40. Bazula, P.A.; Lu, A.H.; Nitz, J.J.; Schüth, F. Surface and pore structure modification of ordered mesoporous carbons via a chemical oxidation approach. *Microporous Mesoporous Mater.* **2008**, *108*, 266–275. [[CrossRef](#)]
41. Kathi, J.; Rhee, K.Y. Surface modification of multi-walled carbon nanotubes using 3-aminopropyltriethoxysilane. *J. Mater. Sci.* **2008**, *43*, 33–37. [[CrossRef](#)]
42. Roggenbuck, J.; Waitz, T.; Tiemann, M. Synthesis of mesoporous metal oxides by structure replication: Strategies of impregnating porous matrices with metal salts. *Microporous Mesoporous Mater.* **2008**, *113*, 575–582. [[CrossRef](#)]
43. Velasco-Santos, C.; Martínez-Hernández, A.L.; Lozada-Cassou, M.; Alvarez-Castillo, A.; Castaño, V.M. Chemical functionalization of carbon nanotubes through an organosilane. *Nanotechnology* **2002**, *13*, 495–498. [[CrossRef](#)]
44. Budarin, V.; Clark, J.H.; Hardy, J.J.E.; Luque, R.; Milkowski, K.; Tavener, S.J.; Wilson, A.J. Starbons: New starch-derived mesoporous carbonaceous materials with tunable properties. *Angew. Chem. Int. Ed.* **2006**, *45*, 3782–3786. [[CrossRef](#)] [[PubMed](#)]
45. Piech, R.; Kubiak, W.W. Determination of trace arsenic with DDTC-Na by cathodic stripping voltammetry in presence of copper ions. *J. Electroanal. Chem.* **2007**, *599*, 59–64. [[CrossRef](#)]
46. Pallier, V.; Serpaud, B.; Feuillade-Cathalifaud, G.; Bollinger, J.C. Comparison of voltammetric and AAS methods for As (III) quantification in presence of iron species in model water samples with a low mineral content. *J. Environ. Anal. Chem.* **2011**, *91*, 1–16. [[CrossRef](#)]
47. Barra, C.M.; Correia Dos Santos, M.M. Speciation of inorganic arsenic in natural waters by square-wave cathodic stripping voltammetry. *Electroanalysis* **2001**, *13*, 1098–1104. [[CrossRef](#)]
48. Bourlinos, A.B.; Karakassides, M.A.; Stathi, P.; Deligiannakis, Y.; Zboril, R.; Dallas, P.; Steriotis, T.A.; Stubos, A.K.; Trapalis, C. Pyrolytic formation of a carbonaceous solid for heavy metal adsorption. *J. Mater. Sci.* **2011**, *46*, 975–982. [[CrossRef](#)]
49. Lua, A.C.; Yang, T. Effect of activation temperature on the textural and chemical properties of potassium hydroxide activated carbon prepared from pistachio-nut shell. *J. Colloid Interface Sci.* **2004**, *274*, 594–601. [[CrossRef](#)]
50. Schutte, C.J.H.; Buijs, K. The infra-red spectra of K_2CO_3 and its hydrates. *Spectrochim. Acta* **1961**, *17*, 921–926. [[CrossRef](#)]
51. Morterra, C.; Low, M.J.D. IR studies of carbons-VI. The effects of KHCO_3 on cellulose pyrolysis and char oxidation. *Carbon* **1985**, *23*, 335–341. [[CrossRef](#)]
52. Gao, Y.; Yue, Q.; Gao, B.; Li, A. Insight into activated carbon from different kinds of chemical activating agents: A review. *Sci. Total Environ.* **2020**, *746*, 141094. [[CrossRef](#)]
53. Chen, W.; Gong, M.; Li, K.; Xia, M.; Chen, Z.; Xiao, H.; Fang, Y.; Chen, Y.; Yang, H.; Chen, H. Insight into KOH activation mechanism during biomass pyrolysis: Chemical reactions between O-containing groups and KOH. *Appl. Energy* **2020**, *278*, 115730. [[CrossRef](#)]
54. Li, Y.-S.; Church, J.S.; Woodhead, A.L. Infrared and Raman spectroscopic studies on iron oxide magnetic nano-particles and their surface modifications. *J. Magn. Magn. Mater.* **2012**, *324*, 1543–1550. [[CrossRef](#)]
55. Zhang, X.; Yan, Q.; Li, J.; Zhang, J.; Cai, Z. Catalysts on Formation of Carbon-Encapsulated Iron Nanoparticles from Kraft Lignin. *Materials* **2018**, *11*, 139. [[CrossRef](#)] [[PubMed](#)]
56. Guo, X.; Liu, A.; Lu, J.; Niu, X.; Jiang, M.; Ma, Y.; Liu, X.; Li, M. Adsorption Mechanism of Hexavalent Chromium on Biochar: Kinetic, Thermodynamic, and Characterization Studies. *ACS Omega* **2020**, *5*, 27323–27331. [[CrossRef](#)] [[PubMed](#)]
57. Chen, M.; He, F.; Hu, D.; Bao, C.; Huang, Q. Broadened operating pH range for adsorption/reduction of aqueous Cr (VI) using biochar from directly treated jute (*Corchorus capsularis* L.) fibers by H_3PO_4 . *Chem. Eng. J.* **2020**, *381*, 122739. [[CrossRef](#)]
58. Qiu, Y.; Zhang, Q.; Gao, B.; Li, M.; Fan, Z.; Sang, W.; Hao, H.; Wei, X. Removal mechanisms of Cr (VI) and Cr (III) by biochar supported nanosized zero-valent iron: Synergy of adsorption, reduction and transformation. *Environ. Pollut.* **2020**, *265*, 115018. [[CrossRef](#)] [[PubMed](#)]
59. Kong, X.; Han, Z.; Zhang, W.; Song, L.; Li, H. Synthesis of zeolite-supported microscale zero-valent iron for the removal of Cr^{6+} and Cd^{2+} from aqueous solution. *J. Environ. Manag.* **2016**, *169*, 84–90. [[CrossRef](#)] [[PubMed](#)]
60. Liu, Z.; Sawakami, M.; Takaoka, H.; Masuyama, K.; Tsuchiya, K.; Umemoto, M. Characterization of bulk cementite and effect of alloy additions. *Int. J. Mater. Prod. Tech.* **2001**, *SPM1*, 415–420.

61. Franken, L.E.; Grünewald, K.; Boekema, E.J.; Stuart, M.C.A. A Technical Introduction to Transmission Electron Microscopy for Soft-Matter: Imaging, Possibilities, Choices, and Technical Developments. *Small* **2020**, *16*, 1906198. [[CrossRef](#)]
62. Defilippi, C.; Mukadam, M.O.; Nicolae, S.A.; Lees, M.R.; Giordano, C. Iron Carbide@Carbon Nanocomposites: A Tool Box of Functional Materials. *Materials* **2019**, *12*, 323. [[CrossRef](#)]
63. Misof, B.; Roschger, P.; Fratzl, P. Imaging Mineralized Tissues in Vertebrates. *Compr. Biomater.* **2011**, *3*, 407–426. [[CrossRef](#)]
64. Androustopoulos, G.P.; Salmas, C.E. A New Model for Capillary Condensation–Evaporation Hysteresis Based on a Random Corrugated Pore Structure Concept: Prediction of Intrinsic Pore Size Distributions. 1. Model Formulation. *Ind. Eng. Chem. Res.* **2000**, *39*, 3747–3763. [[CrossRef](#)]
65. Androustopoulos, G.P.; Salmas, C.E. A New Model for Capillary Condensation–Evaporation Hysteresis Based on a Random Corrugated Pore Structure Concept: Prediction of Intrinsic Pore Size Distribution. 2. Model Application. *Ind. Eng. Chem. Res.* **2000**, *39*, 3764–3777. [[CrossRef](#)]
66. Chen, S.G.; Yang, R.T. Theoretical Basis for the Potential Theory Adsorption Isotherms. The Dubinin-Radushkevich and Dubinin-Astakhov Equations. *Langmuir* **1994**, *10*, 4244–4249. [[CrossRef](#)]
67. Jagiello, J.; Thommes, M. Comparison of DFT characterization methods based on N₂, Ar, CO₂, and H₂ adsorption applied to carbons with various pore size distributions. *Carbon* **2004**, *42*, 1227–1232. [[CrossRef](#)]
68. Salmas, C.E.; Androustopoulos, G.P. Rigid Sphere Molecular Model Enables an Assessment of the Pore Curvature Effect upon Realistic Evaluations of Surface Areas of Mesoporous and Microporous Materials. *Langmuir* **2005**, *21*, 11146–11160. [[CrossRef](#)] [[PubMed](#)]
69. Greenwood, N.N.; Gibb, T.C. *Mössbauer Spectroscopy*; Chapman & Hall: London, UK, 1971.
70. Ulyanov, A.; Chulkina, A.; Volkov, V.; Zagainov, A.; Protasov, A. Structure and Magnetic Hysteresis Properties of the Mn-Doped (Fe_{0.94}Mn_{0.06})₃ C Cementite. *Metallofiz. Noveishie Tekhnologii* **2011**, *33*, 1613–1625.
71. Zhou, X.L.; Han, K.; Ren, Z.M.; Li, Z. Magnetic Field-Induced Granular Pearlite at Early Stages of Phase Transformation. *Adv. Mat. Res.* **2013**, *650*, 178–184. [[CrossRef](#)]
72. Clint, S.; Chintanapalli, V. A diffusion-chemisorption kinetic model for simulating biosorption using forest macro-fungus, *fomes fasciatus*. *Int. Res. J. Plant Sci.* **2018**, *1*, 107–117. [[CrossRef](#)]
73. Hubbe, M.A.; Azizian, S.; Douven, S. Implications of apparent pseudo-second-order adsorption kinetics onto cellulosic materials. A review. *BioResources* **2019**, *14*, 7582–7626. [[CrossRef](#)]
74. Perlach, J.R. *Activated Carbon Adsorption for Wastewater Treatment*; CRC Press: Boca Raton, FL, USA, 1981; p. 260.
75. Huang, L.; Zhou, S.; Jin, F.; Huang, J.; Bao, N. Characterization and mechanism analysis of activated carbon fiber felt-stabilized nanoscale zero-valent iron for the removal of Cr(VI) from aqueous solution. *Colloids Surf. A* **2014**, *447*, 59–66. [[CrossRef](#)]
76. Mortazavian, S.; An, H.; Chun, D.; Moon, J. Activated carbon impregnated by zero-valent iron nanoparticles (AC/nZVI) optimized for simultaneous adsorption and reduction of aqueous hexavalent chromium: Material characterizations and kinetic studies. *Chem. Eng. J.* **2018**, *353*, 781–795. [[CrossRef](#)]
77. Xu, C.-H.; Zhu, L.-J.; Wang, X.-H.; Lin, S.; Chen, Y.-M. Fast and Highly Efficient Removal of Chromate from Aqueous Solution Using Nanoscale Zero-Valent Iron/Activated Carbon (NZVI/AC). *Water Air Soil Pollut.* **2014**, *225*, 1845. [[CrossRef](#)]
78. Hamadi, N.K.; Chen, X.D.; Farid, M.M.; Lu, M.G.Q. Adsorption kinetics for the removal of chromium (VI) from aqueous solution by adsorbents derived from used tyres and sawdust. *Chem. Eng. J.* **2001**, *84*, 95–105. [[CrossRef](#)]
79. Jiao, C.; Tan, X.; Lin, A.; Yang, W. Preparation of Activated Carbon Supported Bead String Structure Nano Zero Valent Iron in a Polyethylene Glycol-Aqueous Solution and Its Efficient Treatment of Cr (VI) Wastewater. *Molecules* **2020**, *25*, 47. [[CrossRef](#)]
80. Ahmad, W.; Qaiser, S.; Ullah, R.; Mohamed Jan, B.; Karakassides, M.A.; Salmas, C.E.; Kenanakis, G.; Ikram, R. Utilization of Tires Waste-Derived Magnetic-Activated Carbon for the Removal of Hexavalent Chromium from Wastewater. *Materials* **2021**, *14*, 34. [[CrossRef](#)]
81. Nethaji, S.; Sivasamy, A.; Mandal, A.B. Preparation and characterization of corn cob activated carbon coated with nano-sized magnetite particles for the removal of Cr (VI). *Bioresour. Technol.* **2013**, *134*, 94–100. Available online: <https://www.sciencedirect.com/science/article/pii/S0960852413002265> (accessed on 31 August 2021). [[CrossRef](#)] [[PubMed](#)]
82. Kakavandi, B.; Kalantary, R.R.; Farzadkia, M.; Mahvi, A.H.; Esrafil, A.; Azari, A.; Yari, A.R.; Javid, A.B. Enhanced chromium (VI) removal using activated carbon modified by zero valent iron and silver bimetallic nanoparticles. *J. Environ. Health Sci. Eng.* **2014**, *12*, 115. [[CrossRef](#)] [[PubMed](#)]
83. Lv, X.; Xu, J.; Jiang, G.; Tang, J.; Xu, X. Highly active nanoscale zero-valent iron (nZVI)–Fe₃O₄ nanocomposites for the removal of chromium (VI) from aqueous solutions. *J. Colloid Interface Sci.* **2012**, *369*, 460–469. [[CrossRef](#)] [[PubMed](#)]
84. Hu, J.; Lo, I.M.C.; Chen, G. Performance and mechanism of chromate (VI) adsorption by δ-FeOOH-coated maghemite (γ-Fe₂O₃) nanoparticles. *Sep. Purif. Technol.* **2007**, *58*, 76–82. [[CrossRef](#)]
85. Jung, C.; Heo, J.; Han, J.; Her, N.; Lee, S.-J.; Oh, J.; Ryu, J.; Yoon, Y. Hexavalent chromium removal by various adsorbents: Powdered activated carbon, chitosan, and single/multi-walled carbon nanotubes. *Sep. Purif. Technol.* **2013**, *106*, 63–71. [[CrossRef](#)]
86. Karthikeyan, T.; Rajgopal, S.; Miranda, L.R. Chromium (VI) adsorption from aqueous solution by Hevea Brasilinesis sawdust activated carbon. *J. Hazard. Mater.* **2005**, *124*, 192–199. [[CrossRef](#)]
87. Selvi, K.; Pattabhi, S.; Kadirvelu, K. Removal of Cr (VI) from aqueous solution by adsorption onto activated carbon. *Bioresour. Technol.* **2001**, *80*, 87–89. [[CrossRef](#)]

88. Yang, J.; Yu, M.; Chen, W. Adsorption of hexavalent chromium from aqueous solution by activated carbon prepared from longan seed: Kinetics, equilibrium and thermodynamics. *J. Ind. Eng. Chem.* **2015**, *21*, 414–422. [[CrossRef](#)]
89. Ranganathan, K. Chromium removal by activated carbons prepared from *Casurina equisetifolia* leaves. *Bioresour. Technol.* **2000**, *73*, 99–103. [[CrossRef](#)]
90. Asimakopoulos, G.; Baikousi, M.; Salmas, C.; Bourlinos, A.B.; Zboril, R.; Karakassides, M.A. Advanced Cr(VI) sorption properties of activated carbon produced via pyrolysis of the “*Posidonia oceanica*” seagrass. *J. Hazard. Mater.* **2021**, *405*, 124274. [[CrossRef](#)] [[PubMed](#)]
91. Asimakopoulos, G.; Baikousi, M.; Kostas, V.; Papantoniou, M.; Bourlinos, A.B.; Zbořil, R.; Karakassides, M.A.; Salmas, C.E. Nanoporous Activated Carbon Derived via Pyrolysis Process of Spent Coffee: Structural Characterization. Investigation of Its Use for Hexavalent Chromium Removal. *Appl. Sci.* **2020**, *10*, 8812. [[CrossRef](#)]
92. Liu, D.-H.; Guo, Y.; Zhang, L.-H.; Li, W.-C.; Sun, T.; Lu, A.-H. Switchable Transport Strategy to Deposit Active Fe/Fe₃C Cores into Hollow Microporous Carbons for Efficient Chromium Removal. *Small* **2013**, *9*, 3852–3857. [[CrossRef](#)] [[PubMed](#)]
93. Cui, Y.; He, H.; Atkinson, J.D. Iron/Carbon Composites for Cr(VI) Removal Prepared from Harmful Algal Bloom Biomass via Metal Bioaccumulation or Biosorption. *ACS Sustain. Chem. Eng.* **2019**, *7*, 1279–1288. [[CrossRef](#)]